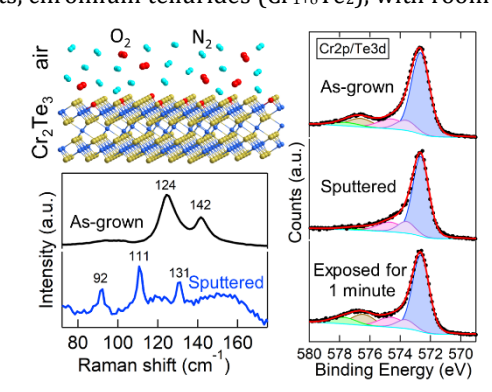
Extreme Air-Sensitivity and Non-Self-Limited Oxidation of Two-Dimensional Magnetic Tellurides

Amanda L. Coughlin, ¹ Jun-Jie Zhang, ² Sammy Bourji, ³ Bingqiang Wei, ⁴ Gaihua Ye, ⁵ Zhipeng Ye, ⁵ Jeonghoon Hong,¹ Tongxie Zhang,¹ Magda Andrade,¹ Xun Zhan,⁶ Rui He,⁵ Jian Wang,⁴ Boris Yakobson,² Yaroslav Losovyj,^{7,8} Ching-Wu Chu,³ Liangzi Deng,³ Shixiong Zhang^{1,9*}

- Department of Physics, Indiana University, Bloomington, Indiana 47405, United States
- Department of Materials Science and NanoEngineering, Rice University, Houston, TX 77005, United States
- Texas Center for Superconductivity and Department of Physics, University of Houston, Houston, TX 77204, United 3.
- Department of Mechanical and Materials Engineering, University of Nebraska, Lincoln, NE 68588, United States
- Department of Electrical and Computer Engineering, Texas Tech University, Lubbock, Texas 79409, United States
- Electron Microscopy Center, Indiana University, Bloomington, Indiana 47405, United States
- 7. Department of Chemistry, Indiana University, Bloomington, Indiana 47405, United States
- 8. Department of Physics and Astronomy, University of Nebraska, Lincoln, NE 68588, US
- Quantum Science and Engineering Center, Indiana University, Bloomington, IN 47405, United States

ABSTRACT: The two-dimensional (2D) self-intercalated van der Waals magnets, chromium tellurides (Cr₁₊₈Te₂), with room temperature ferromagnetism and exotic topological spin textures, have emerged as an attractive platform for the development of ultra-thin spintronic devices. While many prior studies claim $Cr_{1+\delta}Te_2$ are air-stable, which is crucial for practical applications, we demonstrate that within only minutes of exposure to air, dramatic changes occur in the Raman and X-ray photoelectron spectroscopy spectra of nanoplates at room temperature. Time-dependent magnetization measurements and transmission electron microscopy studies suggested the rapid oxidation is not self-limited and has distinct processes on the surfaces and edges. Density functional theory calculations confirmed the spontaneous oxygen adsorption on the surface and the thermodynamically favorable oxidation process. These findings demonstrate unambiguously that the surface of $Cr_{1+\delta}Te_2$ is extremely air-sensitive, highlighting the necessity of surface protection for fundamental studies of intrinsic 2D magnetism and practical applications of advanced spintronic devices.



Atomically thin layers of van der Waals (vdW) magnetic materials create a fertile playground for the fundamental study of two-dimensional (2D) magnetism and open great opportunities for the invention of ultra-thin, all-vdW integrated spintronic devices for information storage and beyond.1-7 Immediately following the discovery of 2D Cr₂Ge₂Te₆⁸ and CrI₃, significant progress was made in developing high-performance spintronic devices, including spin-filter magnetic tunneling junctions^{7, 10, 11} and spin tunnel field-effect transistors,12,13 all of which are made of vdW heterostructures. Despite these exciting advancements, there are still challenges that must be overcome before practical applications are accessible: many vdW magnets 1) have magnetic ordering temperatures well below room

temperature and 2) lack chemical stability under ambient conditions.14

Very recently, chromium tellurides ($Cr_{1+\delta}Te_2$) have emerged as a promising family of self-intercalated vdW magnets which possess considerable potential to address the above challenges. 15-41 CrTe2 (without Cr intercalants) has been reported to host long-range ferromagnetic order up to ~310 K.^{27, 37} The magnetic properties of the system can be effectively tuned by the intercalation of Cr in the vdW gap, by the reduction of thickness down to the 2D limit, 18, 33, ⁴² and by the creation of twisted vdW superstructures.²¹ Beyond robust ferromagnetism, many Cr_{1+δ}Te₂ compounds and their heterostructures have shown signatures of magnetic skyrmions up to room temperature as evidenced

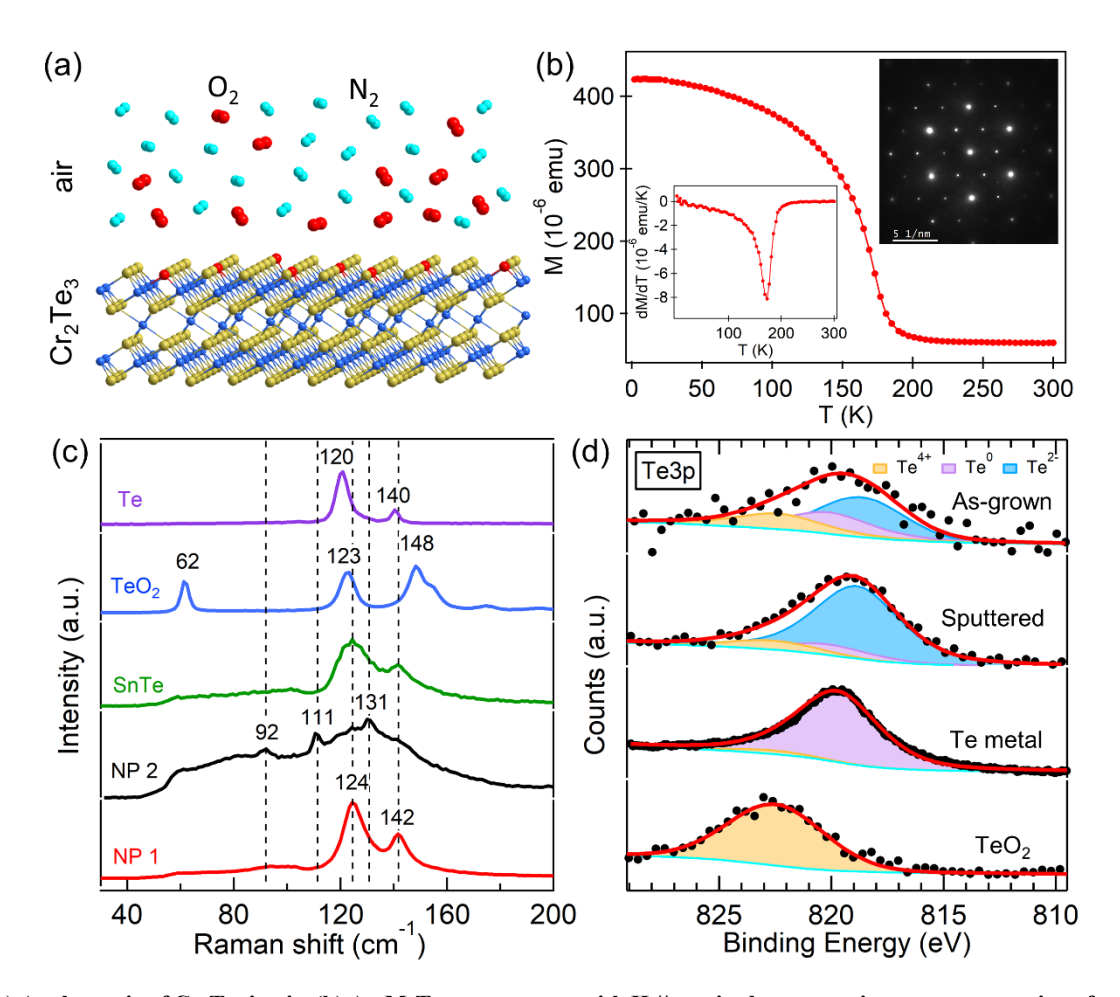


Figure 1. (a) A schematic of Cr_2Te_3 in air. (b) An M-T measurement with H // c-axis, demonstrating a paramagnetic to ferromagnetic transition at ~171 K, as indicated by the dM/dT curve (bottom inset), characteristic of Cr_2Te_3 . The SAED pattern measured along the [001] zone axis of a nanoplate (from the same sample as the magnetization measurements) corresponds to the Cr_2Te_3 phase (top inset). (c) From bottom to top: The two unpolarized Raman spectra (NP 1 and 2) of thin and thick nanoplates, respectively, within minutes after removing them from the growth chamber, SnTe powder, bulk TeO_2 , and freshly cleaved bulk Te metal. (d) XPS scans of the $Te3p_{3/2}$ region of the as-grown nanoplates within 15 minutes of being removed from the growth chamber and after being sputtered, as well as measurements of standard bulk Te metal and TeO_2 .

by the topological Hall effect (THE) $^{43-48}$ and direct visualization via Lorentz transmission electron microscopy (TEM). 17 , 49 , 50 The realization of room temperature skyrmions may pave the way toward the development of vdW-integrated racetrack memory devices for next-generation information technology.

Furthermore, many reports suggest that $Cr_{1+\delta}Te_2$ possess excellent stability in air, mainly based on Raman spectroscopy and X-ray photoelectron spectroscopy (XPS) studies. $^{16-19, 22, 25, 26, 32, 51}$ A Raman spectrum consisting of two characteristic peaks ($\sim 124~cm^{-1}$ and $\sim 142~cm^{-1}$) is reportedly unchanged throughout prolonged periods in air and has been observed in different chromium tellurides, despite their subtle structural differences, as well as in other Tebased chalcogenides of completely different structures, such as SnTe. 52,53 Additionally, the analysis of the XPS spectra for these compounds is complicated since chromium and tellurium each exhibit very closely overlapping peaks, which can lead to large uncertainties in the fitting. Given the lack of disparity between the Raman spectra of reported

 $Cr_{1+\delta}Te_2$ and other telluride compounds, as well as the necessary complexity of the XPS fitting, the overall question of whether the $Cr_{1+\delta}Te_2$ are air-stable requires further examination.

Here, we have performed systematic studies on the stability of a representative chromium telluride, Cr_{1.33}Te₂ [or Cr₂Te₃, Figure 1(a)], by extensive Raman spectroscopy, time-dependent XPS, TEM, and bulk magnetic measurements followed by density functional theory (DFT) calculations. In contrast to previous claims, we unambiguously demonstrate a rapid surface oxidation of chromium telluride within minutes of exposure to air at room temperature and a non-self-limited nature of the oxidation process, which greatly impacts the magnetic properties.

The Cr_2Te_3 nanoplates were grown via chemical vapor deposition (Section S1 in the Supporting Information), and the phase was verified through magnetization studies, which show a paramagnetic to ferromagnetic transition at \sim 171 K [Figure 1(b)], as well as TEM selected area electron diffraction (SAED) studies along the [001] zone axis of a

nanoplate [Figure 1(b) inset], both of which are characteristic of Cr2Te3. Within minutes after removal from the growth chamber, two different Raman spectra were observed in ambient conditions [Figure 1(c)]; Raman peaks were located at \sim 124 and 142 cm⁻¹ or at \sim 92, 111, and 131 cm⁻¹ for typically thinner (NP1, ~9 nm thick) or thicker (NP2, ~18 nm thick) nanoplates, respectively. As previously discussed, the NP1 spectrum matches with peaks reported for various $Cr_{1+\delta}Te_2$ phases ($CrTe_3^{34}Cr_5Te_8^{16}$ and $CrTe_2^{18,27}$), as well as SnTe [Figure 1(c)], which has a completely different structure. This indicates the NP1 spectrum is likely not intrinsic to any $Cr_{1+\delta}Te_2$ phase but characteristic of another structure which forms on the surfaces of Te-based chalcogenides. Figure 1(c) also shows the Raman spectra of bulk TeO₂ and Te; TeO₂ modes are not clearly observed in either NP1 or NP2, and the bulk Te peaks are slightly lower in frequency than NP1. Thin layers of Te (tellurene), however, exhibit blue-shifted peaks (from bulk Te) at ~124 and 142 cm⁻¹ 1.54-56 Thus, the NP1 spectrum reveals that the degraded surface layer contains tellurene. Indeed, the tellurene Raman signal dominates over the other compounds due to the combination of a small band gap and a large Raman scattering cross-section. ⁵⁶ Conversely, the peaks located at \sim 92, 111, and 131 cm⁻¹ (NP2) are the intrinsic Raman peaks of Cr₂Te₃, as demonstrated below. The intrinsic peaks are typically observed in thick nanoplates, as there is likely a larger volume of non-oxidized Cr2Te3 bulk below the degraded surface component, in comparison to thin nanoplates.

Detailed XPS studies were performed on the as-grown (exposed to air for less than 15 minutes) Cr₂Te₃ nanoplates to confirm the existence of a degraded nanoplate surface. We first examined the Te3p_{3/2} core level spectrum, which does not overlap with any Cr core level spectra to unambiguously characterize the oxidation states of Te. As shown in Figure 1(d), the Te3p_{3/2} spectrum of the as-grown nanoplates can be decomposed into three components: ~822.3 eV, ~820.2 eV, and a lower energy component at ~818.6 eV, corresponding to the Te2- state in Cr2Te3. XPS measurements performed on Te standards [Figure 1(d), Figure S7(e)] demonstrate that the ${\sim}822.3$ eV peak is due to $Te^{4{\text +}}$ and the ~820.2 eV peak is due to Te^{0,57} suggesting the oxidation of Cr₂Te₃ progresses through Te⁰ leading to Te⁴⁺ (TeO₂), similar to the oxidation process of SnTe. ^{53, 58, 59} This is consistent with the aforementioned Raman studies, where the tellurene peaks are clearly observed. Raman modes of TeO2 are not clearly observed which may indicate it is amorphous. Further support of the Te and Te oxides is provided by a gentle sputtering experiment (0.5 kV Ar ions for several minutes), which decreases the intensity of the Te4+ and Te0 components and increases the intensity of Te2-[Figure 1(d)], demonstrating the partial removal of the oxidized species from the surface. The high sensitivity of the Cr₂Te₃ nanoplates to ambient conditions is therefore substantiated, as the surface oxides were formed within minutes of exposure to air after the growth.

Previous XPS studies of $Cr_{1+\delta}Te_2$ have focused on the predominant Cr_2p/Te_3d core level spectra. ^{15, 16, 31, 60, 61} These spectra of our as-grown nanoplates exhibit two significant features located at ~572.7 eV and ~576.4 eV [top panel,

Figure 2(a)]. While previous studies have attributed these peaks to the Te3d_{5/2} and Cr2p_{3/2} orbitals of Cr_{1+ δ}Te₂, respectively, the second panel of Figure 2(a) shows that sputtering almost removes the ~576.4 eV peak, and it also increases photoemission in the 572.7 eV area (by $\sim 1.5x$), indicating the removal of surface oxides. Similarly, gentle sputtering significantly reduces the intensity of the higher binding energy part of the Cr2s [Figure 2(b)] transitions. The measured Cr/Te atomic % ratio (at Cr2s and Te3p_{3/2} transitions) for the sputtered nanoplates is 0.67, corresponding to the stoichiometry in Cr2Te3. For the same data points, we ensured the Cr/Te atomic % ratio (0.67) at the Cr2p_{3/2} and $Te3d_{5/2}$ core levels. Deconvolution of that spectra resulted in binding energies for Te^{2-} (~572.7 eV) and Cr^{3+} (~574.7 eV) components and negligible intensity for Te4+ (~576.5 eV) and Cr^{3+} (~577.6 eV) corresponding to TeO_2 and Cr_2O_3 surface oxides, respectively [second panel of Figure 2(a), Table S3]. Given the already complex deconvolution, we used a single envelope to represent the multiplet structure of each Cr3+ component.62 The remaining intensity in the $Cr2p_{3/2}/Te3d_{5/2}$ region requires a single envelope at ~573.6 eV, which can comprise two components. The first component can be attributed to Te⁰ [Figure S4], and the second one can be attributed to the different chemical environments of the atoms at the interface between Te2- in Cr2Te3 and the oxides on the surface [Figure S5]. 63-65 This five-component deconvolution model was applied to the as-grown spectrum [first panel in Figure 2(a), Table 1]. The as-grown spectrum clearly shows contributions from Te⁰, TeO₂, and Cr₂O₃ surface oxides which were formed within minutes of exposure, highlighting the need for passivation techniques such as encapsulation with hBN or graphene, through a dry-stamp method to prevent rapid oxidation. 66-69 The presence of oxides is further supported by the O1s spectra of the nanoplates [Figure S6].

The surface cleaning/oxidation process is reversible and was reproduced several times [third panel of Figure 2(a)]. Further exposure leads to an increased amount of surface oxides, as indicated by the enhanced intensity of Te4+ and Cr³⁺ after 3 h in air [fourth panel of Figure 2(a)]. These nanoplates were remeasured after they had been exposed for ~3 years; the Cr2p/Te3d core level spectrum can be deconvolved into three main components at ~573.0 eV, 576.4 eV, and 577.7 eV [Figure 2(c)], corresponding to Te⁰, TeO₂, and Cr₂O₃, respectively [Figures S7-S8]. This heavily oxidized sample is dominated by Te⁰, and Te⁴⁺ and Cr³⁺ oxides. The signals of Cr3+ and Te2- from Cr2Te3 are attenuated by the probing depth. We estimate the oxide thickness as more than 10 nm, although it can be removed to uncover Cr₂Te₃ underneath via short, gentle Ar sputtering (0.5 kV, 2-5 min). This suggests the surface oxidation of chromium telluride is more complicated and may not be self-limited, unlike in silicon where the growth of native oxides is self-limited to 1-2 nm. 70 It is worth mentioning that chromium exhibits different binding energies for the Cr3+ oxidation states in Cr2O3 (~577.6 eV) and Cr₂Te₃ (~574.6 eV) in our deconvolution model [Figure 2(a)]; this is not uncommon given that the binding energies of the same oxidation state can vary

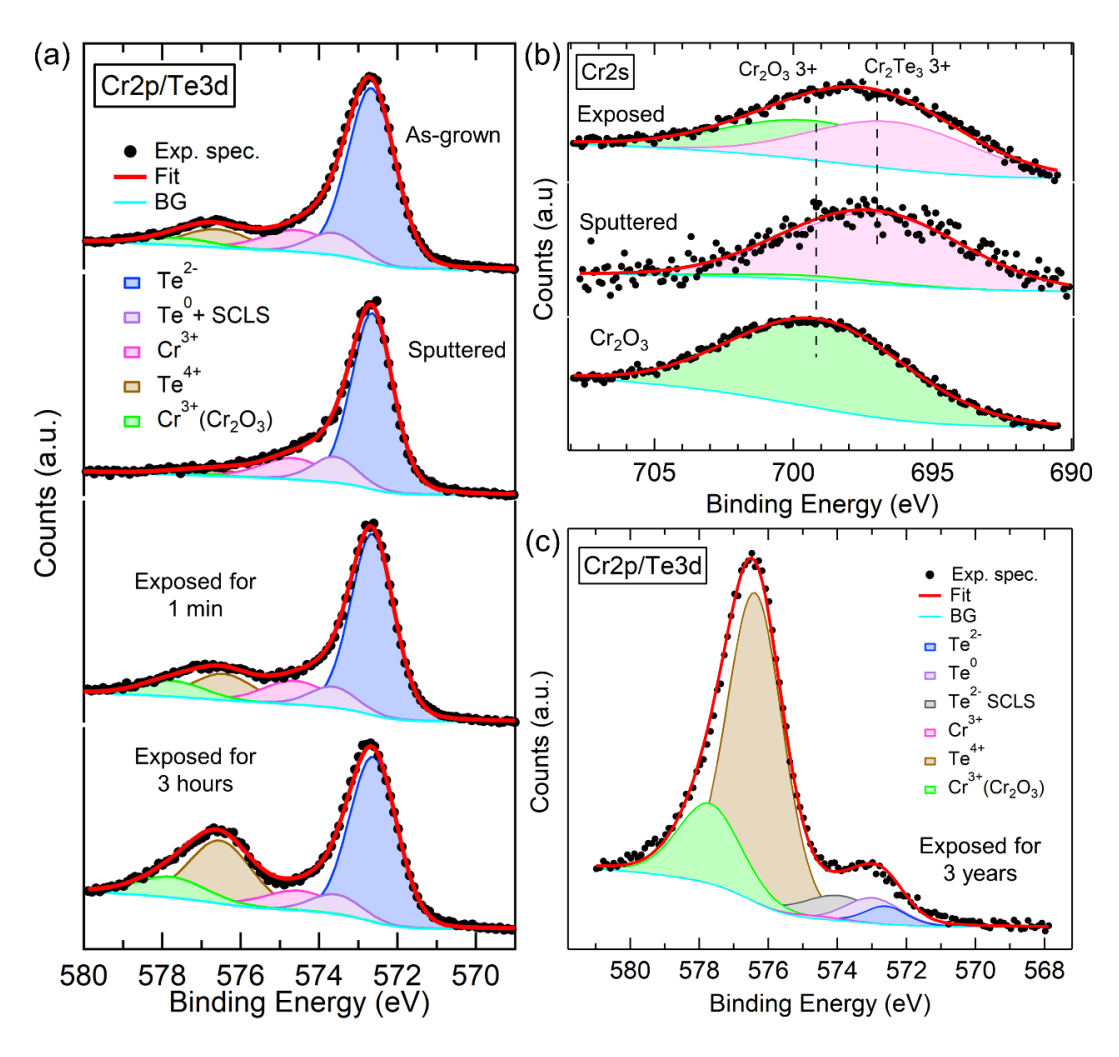


Figure 2. (a) The high-resolution Cr2p/Te3d XPS spectra (from top to bottom) of the as-grown nanoplates 15 min after being exposed to air, gently sputtered nanoplates, nanoplates after being exposed to air for 1 min, nanoplates after being exposed to air for 3 hours. We note the 1 min re-exposure spectrum has slightly more surface oxides than the as-grown spectrum since sputtering creates more surface roughness and dangling bonds, making the nanoplate surface more sensitive to oxidation. (b) The high-resolution scan of the Cr2s region of Cr_2Te_3 nanoplates that have been exposed for an extended period of time, Cr_2Te_3 nanoplates after gentle Ar ion sputtering, and standard Cr_2O_3 powder (from top to bottom). (c) The Cr2p/Te3d XPS spectra of Cr_2Te_3 nanoplates exposed to air for \sim 3 years.

Table 1. The electron binding energies (eV) of the Cr2p/Te3d spectra in Figure 2(a).

	Cr2p _{3/2}		Te3d _{5/2}		
Sample	Cr ³⁺ (Cr ₂ O ₃)	Cr^{3+} (Cr_2Te_3)	Te ²⁻	Te ⁰ +SCLS	Te ⁴⁺
As grown	577.6	574.6	572.7	573.6	576.6
Sputtered	577.6	574.7	572.7	573.6	576.5
1 min exposed	577.7	574.6	572.6	573.6	576.4
3 hours exposed	577.8	574.5	572.6	573.6	576.5

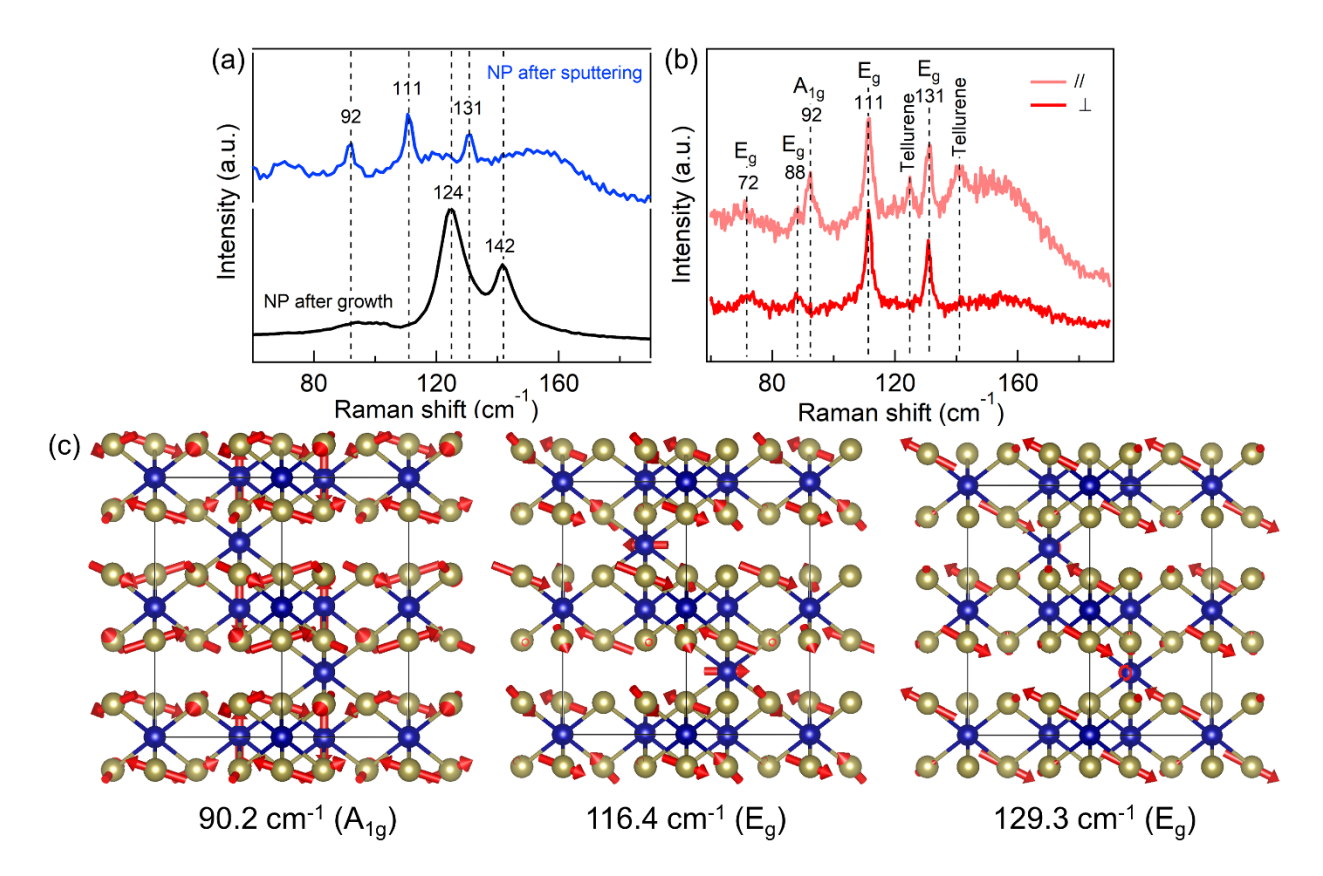


Figure 3. (a) The representative Raman spectra of a Cr_2Te_3 nanoplate that has been exposed to ambient conditions (black spectrum) and a nanoplate after gentle ion sputtering (blue spectrum). (b) Polarized Raman measurements of a Cr_2Te_3 nanoplate with parallel (//) and cross (\bot) polarization orientations. (c) Schematics of the vibrational motions of the 90.2 cm⁻¹ (A_{1g}), 116.4 cm⁻¹ (A_{1g}), and 129.3 cm⁻¹ (A_{1g}) Raman active modes. The A_{1g} mode mainly moves out-of-plane, where the nearest neighbor Te atoms move obliquely in opposite directions at a 120° angle from each other. The two A_{1g} modes are mainly in-plane where the interval Te atoms rotate around the central A_{1g} 0 angle, while the nearest neighbor Te layers move in the opposite direction.

due to differences in the chemical environments. ⁶⁵ Indeed, Cr^{3+} of Cr_2O_3 powder is higher in energy than Cr^{3+} of Cr_2Te_3 in both the Cr2p [Figure S8] and Cr2s core level spectra [Figure 2(b)]. As shown in Figure 2(b), the ~699.2 eV component is Cr_2O_3 based on the standard spectrum in the lower panel, whereas the ~696.4 eV component is from Cr^{3+} in Cr_2Te_3 as it still remains after Ar sputtering, which removes the surface oxides. Therefore, the different binding energies for the same Cr^{3+} oxidation state in our aforementioned deconvolution model is well-justified.

Raman spectroscopy measurements were combined with Ar sputtering to probe the intrinsic vibrational modes of the Cr_2Te_3 nanoplates. Figure 3(a) shows the Raman spectra of an as-grown nanoplate with the two characteristic tellurene peaks and a sputtered nanoplate with peaks at 92, 111, and 131 cm⁻¹. The observation of the latter further demonstrates that sputtering reduces the surface oxides and exposes the Cr_2Te_3 surface, enabling the observation of intrinsic Cr_2Te_3 Raman peaks. Next, we used symmetry group analysis, polarized Raman spectroscopy, and DFT calculations to identify the Raman modes. The nuclear site group analysis of Cr_2Te_3 (space group P-31c) yielded $4A_{1g}$, $4A_{2g}$,

and 9Eg Raman active modes. Polarized Raman measurements were performed on as-grown Cr₂Te₃ nanoplates [Figure 3(b)] in which the depolarization ratio was used to distinguish between the symmetries of the modes. We identify the 92 cm⁻¹ peak as having A_g symmetry and the 72, 88, 111, and 131 cm⁻¹ peaks as having E_g symmetry. DFT calculations of the Cr₂Te₃ Raman frequencies and mode assignments are listed in Table S4. Of the five experimentally observed peaks, the calculated frequencies and mode assignments are 68.6 (E_g), 89.0 (E_g), 90.2 (A_{1g}), 116.4 (E_g), and 129.3 cm⁻ ¹ (E_g), which are close to our observed frequencies and consistent with the assignments from the polarized measurements. The atomic displacements of the three predominant Raman peaks (90.2, 116.4, and 129.3 cm⁻¹) are also determined through the DFT calculations, as shown in Figure 3(c).

Due to the surface degradation, the magnetization of the Cr_2Te_3 nanoplates decreases over successive days of exposure to ambient conditions, although the ferromagnetic transition temperature and coercive field remain nearly constant without a systematic variation [Figure 4(a)-(b)]

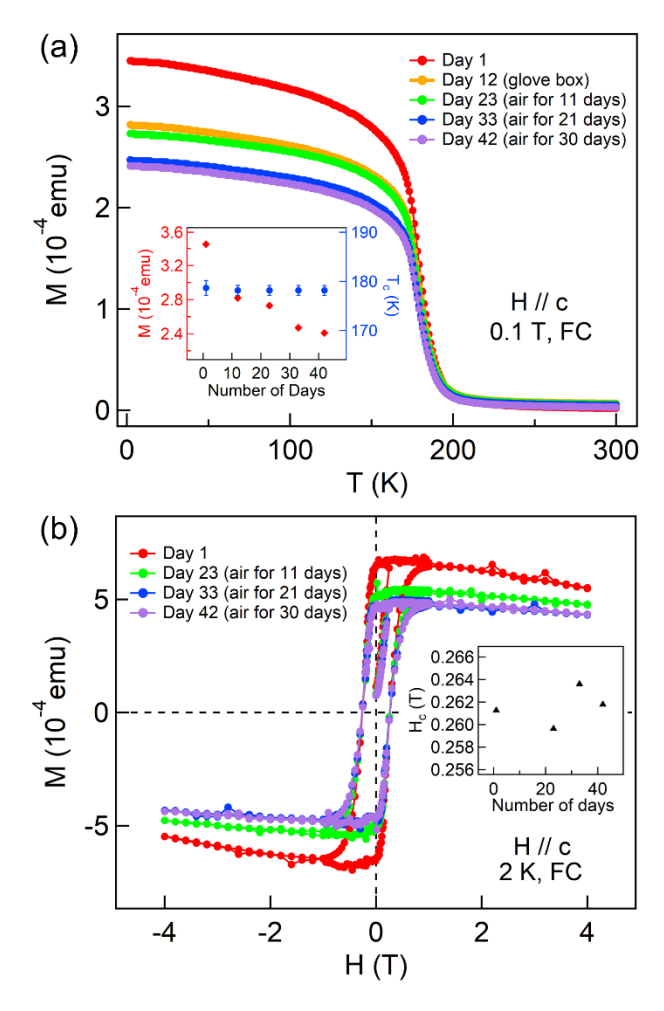


Figure 4. Magnetization studies over time on the same sample as a function of (a) temperature and (b) magnetic field. The inset in (a) shows the M and T_c over time and the inset in (b) shows the H_c over time.

and the insets]. The decline in magnetization as the nanoplates degrade in air can be attributed to the formation of antiferromagnetic Cr_2O_3 (despite minimal uncompensated spins at the boundary 71-73), non-magnetic TeO_2 , and non-magnetic Te components which reduce the overall ferromagnetic signal of the sample. Within the glovebox, oxygen already present on the surface layer of nanoplates from an earlier exposure to air may migrate deeper, react with the ferromagnetic Cr_2Te_3 , and consequently reduce the overall magnetization.

The oxidation process is not self-limited; thus, the magnetization continues to decrease as the amount of antiferromagnetic and non-magnetic surface contributions increase with the thickness of the oxidation layer over time. The degradation process causes a redistribution of valence band density of states, as well (Figures S10-S12).

A prolonged exposure in air also leads to a significant change in structural properties, as evidenced by TEM studies. An SAED pattern of a Cr_2Te_3 nanoplate that was stored in a nitrogen atmosphere [Figure 5(a)] was measured along the [001] zone axis [Figure 5(b)] where sharp diffraction spots indicate the single-crystallinity of the nanoplate. The

characteristic Cr₂Te₃ diffraction spots are indicated by hexagons denoting the {100}, {110}, and {300} planes from the inner to outer hexagons. After exposure for 45 days, new diffraction spots were observed just ~0.1 nm⁻¹ outside of the Cr₂Te₃ {110} spots and are positioned along the pink circle [Figure 5(c), Figure S13]. These new spots do not originate from the surface species that were previously observed in the XPS studies but originate from another phase with a slightly smaller lattice constant than Cr₂Te₃ which we attribute to a Cr₂Te_{3-x}O_v phase, where the increased oxygen concentration reduces the lattice constant due to the smaller ionic radius of oxygen compared to tellurium. Intermediate spots with low intensities were also observed the same distance from the central beam in between the respective Cr₂Te_{3-x}O_v spots and are likely due to the slightly polycrystalline nature of Cr₂Te_{3-x}O_y. Furthermore, a yellow circle indicates another new set of spots appear around each of the Cr₂Te₃ {300} spots due to double diffraction. The absence of clear diffraction spots from surface species (Cr₂O₃, TeO2, Te) previously determined via XPS/Raman is likely because the SAED along the [001] zone axis contains a majority signal from the bulk compared to the negligible surface contribution due to its small volume fraction and polycrystalline/amorphous nature.

In addition to the oxides present on the surfaces, further TEM studies indicate the formation of some other species at the edge. Scanning TEM (STEM) and HAADF-STEM images [Figures 5(d)-(e), respectively], reveal a darker contrast around the edge of the nanoplate. Energy dispersive x-ray spectroscopy (XEDS) maps [Figure 5(f)-(h)] show the nanoplate interior is composed of Cr and Te, as well as O from the previously discussed surface oxides, while the edge contains Cr and Te, and an enhanced O signal. An edge contrast can also be clearly observed in a high-resolution TEM image shown in Figure 5(i).

Fast Fourier transform (FFT) analysis was performed to determine the structural phase of the interior and edge species [Figure 5(j)-(l)]. Figure 5(j) shows the interior of the nanoplate remains consistent with Cr_2Te_3 (red). FFT near the edge of the nanoplate (blue) [Figure 5(k)] demonstrates a diffraction pattern consistent with Te (space group P3₁21) along the [001] zone axis, while another region (green) corresponds to the CrO_2 phase (space group P42/mnm) along [001] [Figure 5(l)]. The formation of metastable CrO_2 is consistent with the increased intensity of the O signal along the edge in the XEDS map. It is worth mentioning that no additional ferromagnetic phases were observed in the magnetization measurements, possibly due to small amounts of CrO_2 below the detection limit of the measurement.

DFT calculations demonstrate that the oxidation of $Cr_{1+\delta}Te_2$ is a thermodynamically favorable process. First, we calculated the bond lengths and adsorption energy of O_2 adsorbed on the surface of Cr_2Te_3 . With the initial distance of 3.00 Å, we found that oxygen molecules could almost parallelly absorb on the surface after lattice relaxation (Figure S14). The calculated 0-0 and Te-0 bond lengths are 1.38 Å and 2.19~2.23 Å, respectively; the adsorption distance is 1.99 Å, and the obtained adsorption energy is -0.11 eV. This suggests that O_2 exhibits a spontaneous adsorption

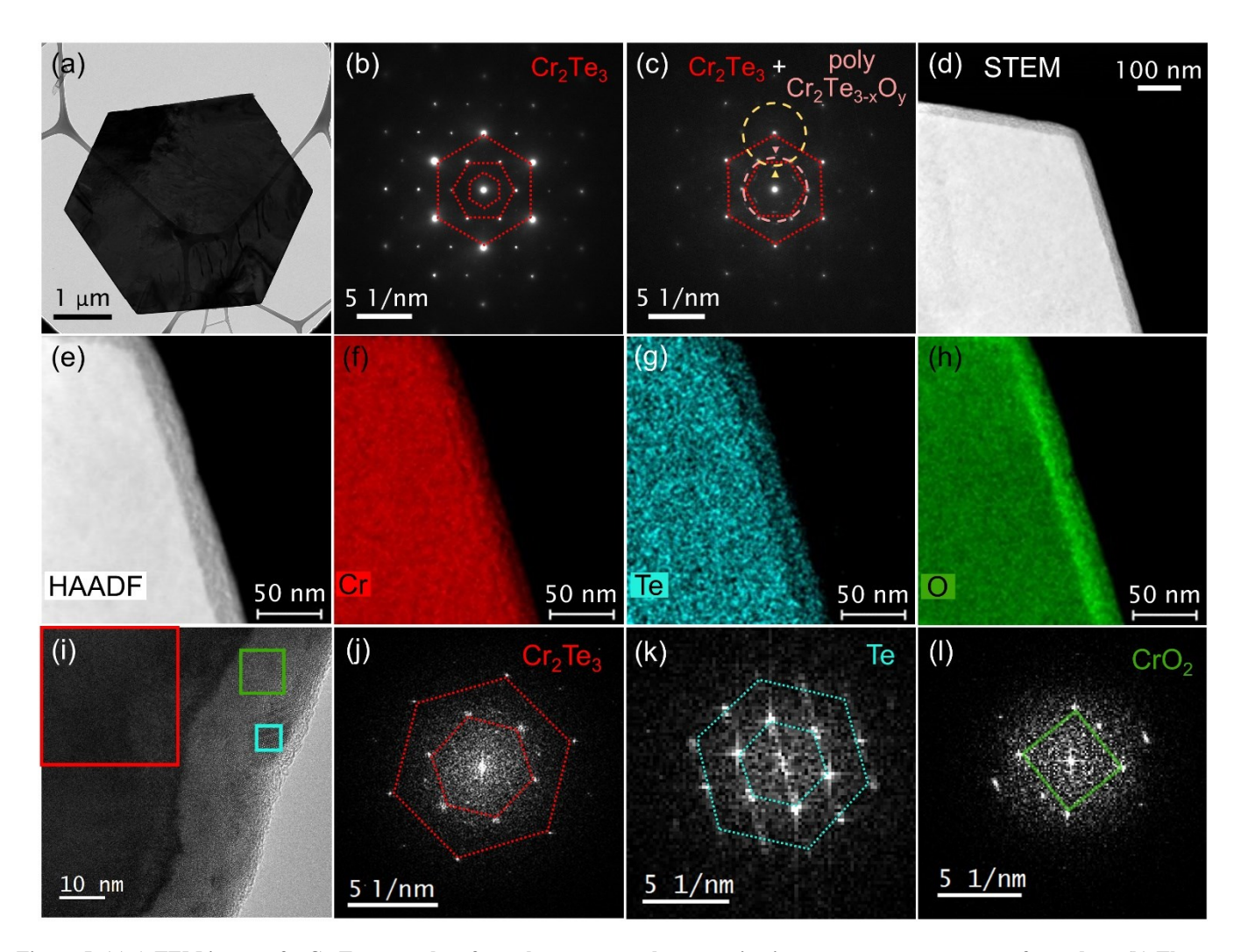


Figure 5. (a) A TEM image of a Cr_2Te_3 nanoplate from the same sample magnetization measurements were performed on. (b) The SAED pattern taken on a single-crystalline Cr_2Te_3 nanoplate and (c) a Cr_2Te_3 /polycrystalline- Cr_2Te_3 - xO_y nanoplate after oxidation, as evidenced by the extra spots indicated by a pink circle slightly larger than the red {110} Cr_2Te_3 hexagon. (d) A STEM image and (e) HAADF image taken on the edge of a nanoplate showing the change in contrast between the interior and edge of the nanoplate. TEM-EDS maps of (f) Cr, (g) Te, and (h) O along the edge of the nanoplate. (i) A high-resolution TEM image of the edge of a nanoplate with respective FFT diffraction patterns from the interior area (j) shown within the red square, characteristic of Cr_2Te_3 and (k)-(l) shown within the blue and green squares near the edge, characteristic of Te and Te0, respectively. The extra spots in the Te0 Te1 are from an overlap with a region containing Te1.

Table 2. The differences in formation energies for various chromium telluride (Cr_xTe_y) phases reacting with O_2 leading to the production of either Cr_2O_3 and TeO_2 (top) or CrO_2 and Te (bottom).

Oxidation Products	Cr_2Te_3	Cr_1Te_2	Cr ₅ Te ₈	$\operatorname{Cr_3Te_4}$	Cr ₁ Te ₁
Te and CrO ₂	-2.17 eV	-1.43 eV	-1.76 eV	-2.27 eV	-3.25 eV
$\operatorname{Cr_2O_3}$ and $\operatorname{TeO_2}$	-6.35 eV	-4.90 eV	-5.88 eV	-6.57 eV	-7.98 eV

The formation energies are calculated from $\Delta E = \left(\frac{1}{y}\right) C r_x T e_y + \left(\frac{3x}{4y} + 1\right) O_2 - \left[\left(\frac{x}{2y}\right) C r_2 O_3 + T e O_2\right]$ for the top row and $\Delta E = \left(\frac{1}{y}\right) C r_x T e_y + \left(\frac{x}{y}\right) O_2 - \left[T e + \left(\frac{x}{y}\right) C r O_2\right]$ for the bottom row.

on the Cr₂Te₃ surface. Next, we calculated the formation energies of productions resulting from O₂ molecules

adsorbed onto the surface of Cr₂Te₃. Two possible productions from the reaction of Cr₂Te₃ and O₂ are the formation

of CrO₂ and Te (case 1) or Cr₂O₃ and TeO₂ (case 2). The energy difference between the products and reactants (ΔE) was negative, -2.17 eV for case 1 and -6.35 eV for case 2, indicating that both oxidation processes are thermodynamically favorable. The smaller ΔE for case 2 suggests the formation of TeO2 is more favorable than the formation of Te, which is consistent with our XPS studies that demonstrate the majority of the oxide formed after a prolonged exposure in air is TeO2 [Figure 2(c)]. Indeed, the formation of CrO2 and Te is slightly less favorable, as Te is the intermediate state before the transformation into TeO2. The formation energy calculation was extended to other phases of chromium tellurides (Cr_xTe_y), in which the negative formation energies of all phases [Table 2] reveal that chromium tellurides are indeed unstable and spontaneously oxidize when exposed to air. Furthermore, since we have demonstrated that Raman spectroscopy can be used to detect degraded species, other $Cr_{1+\delta}Te_2$ compounds that have been reported to exhibit this same spectrum demonstrate their instability in air and are in agreement with our DFT energy evalua-

In summary, we have systematically demonstrated the high instability of self-intercalated vdW $Cr_{1+\delta}Te_2$ nanoplates under ambient conditions and report the intrinsic Raman spectra of Cr2Te3. Detailed XPS and sputtering measurements confirm the surface fragility of the Cr₂Te₃ nanoplates in air, and the proposed deconvolution model of the closely overlapping Cr2p/Te3d core levels captures their surface sensitive nature. The reduction of magnetization over time is attributed to the formation of antiferromagnetic and nonmagnetic surface species which decreases the ferromagnetic bulk contribution of the Cr₂Te₃ nanoplates. TEM measurements indicate the formation of an additional crystallized phase, as well as distinct oxidation processes along the nanoplate edges and interior regions. DFT calculations suggest that the formation of the aforementioned surface species is a thermodynamically favorable process. Our work therefore demonstrates unambiguously that Cr_{1+δ}Te₂ are not air-stable as previously claimed, highlighting the necessity of surface passivation/protection of this rich family of self-intercalated vdW magnets for both the fundamental studies of intrinsic 2D magnetism and practical applications of advanced spintronic devices.

ASSOCIATED CONTENT

Supporting Information

The preparation of samples for magnetization measurement details; demonstrating the broad shoulder in Raman of oxidized nanoplates may be due to TeO_2 ; the Raman peak intensity of exposed/sputtered nanoplates increases over time; fitting the Cr2p/Te3d spectrum with 6 components; ARXPS of Te^0+SCLS component; the formation of surface oxides reduces the Te^0+SCLS to bulk contribution; HRXPS scans of the Cr_2Te_3 nanoplates and of the standards; DFT calculated Cr_2Te_3 Raman active modes; TEM studies on Cr_2Te_3 nanoplates from the polarized Raman studies; SAED on an additional Cr_2Te_3 nanoplate; DFT calculated structure of O_2 adsorbed onto Cr_2Te_3 . This material is available free of charge via the Internet at http://pubs.acs.org.

AUTHOR INFORMATION

Corresponding Author

*Shixiong Zhang – Department of Physics, Indiana University, Bloomington, Indiana 47405, United States; orcid.org/0000-0002-1004-0597; Email: sxzhang@indiana.edu

Author Contributions

The manuscript was written through contributions of all authors. All authors have given approval to the final version of the manuscript.

Notes

The authors declare no competing financial interest.

ACKNOWLEDGMENTS

We thank Prof. P. Dowben for helpful discussions and Prof. A. Siedle for providing the standard materials for the XPS studies. The work done at Indiana University was mainly supported by the Vice Provost for Research through the Faculty Research Support Program. We also acknowledge support from National Science Foundation through grant nos. ECCS-1936406 (T.X.Z.). US Air Force Office of Scientific Research Grants FA9550-15-1-0236 and FA9550-20-1-0068, the T.L.L. Temple Foundation, the John J. and Rebecca Moores Endowment, and the State of Texas through the Texas Center for Superconductivity at the University of Houston (TcSUH). The work at TTU was supported by NSF CAREER Grant No. DMR-1760668. TEM measurements performed in the Nebraska Center for Materials and Nanoscience was supported by the National Science Foundation under Award ECCS: 1542182. Access to XPS at the Nanoscale Characterization Facility was provided by the NSF Award DMR MRI-1126394.

REFERENCES

- Burch, K. S.; Mandrus, D.; Park, J.-G. Magnetism in Two-Dimensional Van Der Waals Materials. *Nature* 2018, 563, 47-52.
- Kawakami, R. K. Spin and Magnetism in 2d Materials. arXiv preprint arXiv:1911.00894 2019.
- Wang, Q. H.; Bedoya-Pinto, A.; Blei, M.; Dismukes, A. H.; Hamo, A.; Jenkins, S.; Koperski, M.; Liu, Y.; Sun, Q.-C.; Telford, E. J.; Kim, H. H.; Augustin, M.; Vool, U.; Yin, J.-X.; Li, L. H.; Falin, A.; Dean, C. R.; Casanova, F.; Evans, R. F. L.; Chshiev, M.; Mishchenko, A.; Petrovic, C.; He, R.; Zhao, L.; Tsen, A. W.; Gerardot, B. D.; Brotons-Gisbert, M.; Guguchia, Z.; Roy, X.; Tongay, S., et al. The Magnetic Genome of Two-Dimensional Van Der Waals Materials. ACS Nano 2022, 16, 6960-7079.
- Gibertini, M.; Koperski, M.; Morpurgo, A.; Novoselov, K. Magnetic 2d Materials and Heterostructures. *Nat. Nanotechnol.* 2019, 14, 408-419.
- Lin, X.; Yang, W.; Wang, K. L.; Zhao, W. Two-Dimensional Spintronics for Low-Power Electronics. *Nature Electronics* 2019, 2, 274-283.
- Liang, S. J.; Cheng, B.; Cui, X.; Miao, F. Van Der Waals Heterostructures for High-Performance Device Applications: Challenges and Opportunities. Adv. Mater. 2020, 32, 1903800.
- Klein, D. R.; MacNeill, D.; Lado, J. L.; Soriano, D.; Navarro-Moratalla, E.; Watanabe, K.; Taniguchi, T.; Manni, S.; Canfield, P.; Fernández-Rossier, J.; Jarillo-Herrero, P. Probing Magnetism in 2d Van Der Waals Crystalline Insulators Via Electron Tunneling. Science 2018, 360, 1218-1222.

- 8. Gong, C.; Li, L.; Li, Z.; Ji, H.; Stern, A.; Xia, Y.; Cao, T.; Bao, W.; Wang, C.; Wang, Y.; Qiu, Z. Q.; Cava, R. J.; Louie, S. G.; Xia, J.; Zhang, X. Discovery of Intrinsic Ferromagnetism in Two-Dimensional Van Der Waals Crystals. *Nature* **2017**, *546*, 265-269
- 9. Huang, B.; Clark, G.; Navarro-Moratalla, E.; Klein, D. R.; Cheng, R.; Seyler, K. L.; Zhong, D.; Schmidgall, E.; McGuire, M. A.; Cobden, D. H.; Yao, W.; Xiao, D.; Jarillo-Herrero, P.; Xu, X. Layer-Dependent Ferromagnetism in a Van Der Waals Crystal Down to the Monolayer Limit. *Nature* **2017**, *546*, 270-273.
- Song, T.; Cai, X.; Tu, M. W.-Y.; Zhang, X.; Huang, B.; Wilson, N. P.; Seyler, K. L.; Zhu, L.; Taniguchi, T.; Watanabe, K.; McGuire, M. A.; Cobden, D. H.; Xiao, D.; Yao, W.; Xu, X. Giant Tunneling Magnetoresistance in Spin-Filter Van Der Waals Heterostructures. Science 2018, 360, 1214-1218.
- Kim, H. H.; Yang, B.; Patel, T.; Sfigakis, F.; Li, C.; Tian, S.; Lei, H.; Tsen, A. W. One Million Percent Tunnel Magnetoresistance in a Magnetic Van Der Waals Heterostructure. *Nano Lett.* 2018, 18, 4885-4890.
- Jiang, S.; Shan, J.; Mak, K. F. Electric-Field Switching of Two-Dimensional Van Der Waals Magnets. *Nat. Mater.* 2018, 17, 406-410.
- Jiang, S.; Li, L.; Wang, Z.; Shan, J.; Mak, K. F. Spin Tunnel Field-Effect Transistors Based on Two-Dimensional Van Der Waals Heterostructures. *Nature Electronics* 2019, 2, 159-163.
- Shcherbakov, D.; Stepanov, P.; Weber, D.; Wang, Y.; Hu, J.; Zhu, Y.; Watanabe, K.; Taniguchi, T.; Mao, Z.; Windl, W.; Goldberger, J. E.; Bockrath, M.; Lau, C. N. Raman Spectroscopy, Photocatalytic Degradation, and Stabilization of Atomically Thin Chromium Tri-Iodide. *Nano Lett.* 2018, 18, 4214-4219.
- Tang, B. J.; Wang, X. W.; Han, M. J.; Xu, X. D.; Zhang, Z. W.; Zhu, C.; Cao, X.; Yang, Y. M.; Fu, Q. D.; Yang, J. Q.; Li, X. J.; Gao, W. B.; Zhou, J. D.; Lin, J. H.; Liu, Z. Phase Engineering of Cr5te8 with Colossal Anomalous Hall Effect. *Nature Electronics* 2022, 5, 224-232.
- Chen, C.; Chen, X. D.; Wu, C. W.; Wang, X.; Ping, Y.; Wei, X.; Zhou, X.; Lu, J. B.; Zhu, L. J.; Zhou, J. D.; Zhai, T. Y.; Han, J. B.; Xu, H. Air-Stable 2d Cr5te8 Nanosheets with Thickness-Tunable Ferromagnetism. Adv. Mater. 2022, 34, 2107512.
- 17. Li, B.; Deng, X.; Shu, W.; Cheng, X.; Qian, Q.; Wan, Z.; Zhao, B.; Shen, X.; Wu, R.; Shi, S.; Zhang, H.; Zhang, Z.; Yang, X.; Zhang, J.; Zhong, M.; Xia, Q.; Li, J.; Liu, Y.; Liao, L.; Ye, Y.; Dai, L.; Peng, Y.; Li, B.; Duan, X. Air-Stable Ultrathin Cr3te4 Nanosheets with Thickness-Dependent Magnetic Biskyrmions. *Mater. Today* 2022, 57, 66-74.
- Meng, L.; Zhou, Z.; Xu, M.; Yang, S.; Si, K.; Liu, L.; Wang, X.; Jiang, H.; Li, B.; Qin, P.; Zhang, P.; Wang, J.; Liu, Z.; Tang, P.; Ye, Y.; Zhou, W.; Bao, L.; Gao, H.-J.; Gong, Y. Anomalous Thickness Dependence of Curie Temperature in Air-Stable Two-Dimensional Ferromagnetic 1t-Crte 2 Grown by Chemical Vapor Deposition. *Nat. Commun.* 2021, 12, 1-8.
- 19. Wu, H.; Zhang, W.; Yang, L.; Wang, J.; Li, J.; Li, L.; Gao, Y.; Zhang, L.; Du, J.; Shu, H.; Chang, H. Strong Intrinsic Room-Temperature Ferromagnetism in Freestanding Non-Van Der Waals Ultrathin 2d Crystals. *Nat. Commun.* **2021**, *12*, 5688.
- Niu, K.; Qiu, G.; Wang, C.; Li, D.; Niu, Y.; Li, S.; Kang, L.; Cai, Y.; Han, M.; Lin, J. Self-Intercalated Magnetic Heterostructures in 2d Chromium Telluride. Adv. Funct. Mater. 2023, 33, 2208528.
- Coughlin, A. L.; Xie, D.; Zhan, X.; Yao, Y.; Deng, L.; Hewa-Walpitage, H.; Bontke, T.; Chu, C.-W.; Li, Y.; Wang, J.; Fertig, H. A.; Zhang, S. Van Der Waals Superstructure and Twisting in Self-Intercalated Magnet with near Room-Temperature Perpendicular Ferromagnetism. *Nano Lett.* 2021, 21, 9517-9525.
- 22. Jin, Z.; Ji, Z.; Zhong, Y.; Jin, Y.; Hu, X.; Zhang, X.; Zhu, L.; Huang, X.; Li, T.; Cai, X.; Zhou, L. Controlled Synthesis of a Two-

- Dimensional Non-Van Der Waals Ferromagnet toward a Magnetic Moiré Superlattice. *ACS Nano* **2022**, *16*, 7572-7579.
- 23. Huey, W. L.; Ochs, A. M.; Williams, A. J.; Zhang, Y.; Kraguljac, S.; Deng, Z.; Moore, C. E.; Windl, W.; Lau, C. N.; Goldberger, J. E. Cr X Pt1–X Te2 (X≤ 0.45): A Family of Air-Stable and Exfoliatable Van Der Waals Ferromagnets. *ACS nano* **2022**, *16*, 3852-3860.
- 24. Luo, S.; Zhu, X.; Liu, H.; Song, S.; Chen, Y.; Liu, C.; Zhou, W.; Tang, C.; Shao, G.; Jin, Y.; Guan, J.; Tung, V. C.; Li, H.; Chen, X.; Ouyang, F.; Liu, S. Direct Growth of Magnetic Non-Van Der Waals Cr2x3(X = S, Se, and Te) on Sio2/Si Substrates through the Promotion of Koh. *Chem. Mater.* 2022, 34, 2342-2351.
- 25. Gao, Z.; Tang, M.; Huang, J.; Chen, J.; Ai, W.; Wu, L.; Dong, X.; Ma, Y.; Zhang, Z.; Zhang, L.; Du, Y.; Fu, H.; Yuan, H.; Wu, J.; Luo, F. Near Room-Temperature Ferromagnetism in Air-Stable Two-Dimensional Cr1–Xte Grown by Chemical Vapor Deposition. *Nano Research* 2022, 15, 3763-3769.
- Wang, M.; Kang, L.; Su, J.; Zhang, L.; Dai, H.; Cheng, H.; Han, X.; Zhai, T.; Liu, Z.; Han, J. Two-Dimensional Ferromagnetism in Crte Flakes Down to Atomically Thin Layers. *Nanoscale* 2020, 12, 16427-16432.
- 27. Sun, X.; Li, W.; Wang, X.; Sui, Q.; Zhang, T.; Wang, Z.; Liu, L.; Li, D.; Feng, S.; Zhong, S.; Wang, H.; Bouchiat, V.; Regueiro, M. N.; Rougemaille, N.; Coraux, J.; Purbawati, A.; Hadj-Azzem, A.; Wang, Z.; Dong, B.; Wu, X.; Yang, T.; Yu, G.; Wang, B.; Han, Z.; Han, X.; Zhang, Z. Room Temperature Ferromagnetism in Ultra-Thin Van Der Waals Crystals of 1t-Crte2. *Nano Research* 2020, 13, 3358-3363.
- Coughlin, A. L.; Xie, D.; Yao, Y.; Zhan, X.; Chen, Q.; Hewa-Walpitage, H.; Zhang, X.; Guo, H.; Zhou, H.; Lou, J.; Wang, J.; Li, Y. S.; Fertig, H. A.; Zhang, S. Near Degeneracy of Magnetic Phases in Two-Dimensional Chromium Telluride with Enhanced Perpendicular Magnetic Anisotropy. ACS nano 2020, 14, 15256-15266.
- Jeon, J. H.; Na, H. R.; Kim, H.; Lee, S.; Song, S.; Kim, J.; Park, S.; Kim, J.; Noh, H.; Kim, G.; Jerng, S. K.; Chun, S. H. Emergent Topological Hall Effect from Exchange Coupling in Ferromagnetic Cr2te3/ Noncoplanar Antiferromagnetic Cr2se3 Bilayers. Acs Nano 2022, 16, 8974-8982.
- 30. Jiang, Z.; Luo, X.; Yan, J.; Gao, J.; Wang, W.; Zhao, G.; Sun, Y.; Si, J.; Lu, W.; Tong, P.; Zhu, X. B.; Song, W. H.; Sun, Y. P. Magnetic Anisotropy and Anomalous Hall Effect in Monoclinic Single Crystal Cr 5 Te 8. *Phys. Rev. B* 2020, 102, 144433.
- Chua, R.; Zhou, J.; Yu, X. J.; Yu, W.; Gou, J.; Zhu, R.; Zhang, L.; Liu, M. Z.; Breese, M. B. H.; Chen, W.; Loh, K. P.; Feng, Y. P.; Yang, M.; Huang, Y. L.; Wee, A. T. S. Room Temperature Ferromagnetism of Monolayer Chromium Telluride with Perpendicular Magnetic Anisotropy. *Adv. Mater.* 2021, *33*, 2103360.
- 32. Fu, B.; Bao, X.; Deng, H.; Zhang, M. Redetermination the Basic Cell Trigonal Cr5te8 Single Crystal Structure and Its Temperature Dependence Raman Spectra. *J. Solid State Chem.* **2021**, *300*, 122222.
- 33. Zhang, X.; Lu, Q.; Liu, W.; Niu, W.; Sun, J.; Cook, J.; Vaninger, M.; Miceli, P. F.; Singh, D. J.; Lian, S.-W.; Chang, T.-R.; He, X.; Du, J.; He, L.; Zhang, R.; Bian, G.; Xu, Y. Room-Temperature Intrinsic Ferromagnetism in Epitaxial Crte 2 Ultrathin Films. *Nat. Commun.* 2021, 12, 1-9.
- 34. Guo, Y.; Kang, L.; Yu, S.; Yang, J.; Qi, X.; Zhang, Z.; Liu, Z. Cvd Growth of Large-Scale and Highly Crystalline 2d Chromium Telluride Nanoflakes. *ChemNanoMat* 2021, 7, 323-327.
- 35. Huang, Y. L.; Chen, W.; Wee, A. T. Two-Dimensional Magnetic Transition Metal Chalcogenides. *SmartMat* **2021**, *2*, 139-153.
- 36. Wang, Y.; Kajihara, S.; Matsuoka, H.; Saika, B. K.; Yamagami, K.; Takeda, Y.; Wadati, H.; Ishizaka, K.; Iwasa, Y.; Nakano, M. Layer-Number-Independent Two-Dimensional Ferromagnetism in Cr3te4. *Nano Lett.* **2022**, *22*, 9964-9971.
- 37. Freitas, D. C.; Weht, R.; Sulpice, A.; Remenyi, G.; Strobel, P.; Gay, F.; Marcus, J.; Núñez-Regueiro, M. Ferromagnetism in Layered

- Metastable 1t-Crte2. *J. Phys.: Condens. Matter* **2015,** *27,* 176002.
- 38. Liu, Y.; Abeykoon, M.; Stavitski, E.; Attenkofer, K.; Petrovic, C. Magnetic Anisotropy and Entropy Change in Trigonal Cr 5 Te 8. *Phys. Rev. B* **2019**, *100*, 245114.
- 39. Liu, Y.; Petrovic, C. Critical Behavior of the Quasi-Two-Dimensional Weak Itinerant Ferromagnet Trigonal Chromium Telluride Cr 0.62 Te. *Phys. Rev. B* **2017**, *96*, 134410.
- 40. Liu, Y.; Petrovic, C. Anomalous Hall Effect in the Trigonal Cr 5 Te 8 Single Crystal. *Phys. Rev. B* **2018**, *98*, 195122.
- 41. Fujisawa, Y.; Pardo-Almanza, M.; Garland, J.; Yamagami, K.; Zhu, X.; Chen, X.; Araki, K.; Takeda, T.; Kobayashi, M.; Takeda, Y. Tailoring Magnetism in Self-Intercalated Cr 1+ Δ Te 2 Epitaxial Films. *Phys. Rev. Mater.* **2020**, *4*, 114001.
- 42. Wen, Y.; Liu, Z.; Zhang, Y.; Xia, C.; Zhai, B.; Zhang, X.; Zhai, G.; Shen, C.; He, P.; Cheng, R.; Yin, L.; Yao, Y.; Sendeku, M. G.; Wang, Z.; Ye, X.; Liu, C.; Jiang, C.; Shan, C.; Long, Y.; He, J. Tunable Room-Temperature Ferromagnetism in Two-Dimensional Cr2te3. *Nano Lett.* **2020**, *20*, 3130-3139.
- 43. Zhao, D.; Zhang, L.; Malik, I. A.; Liao, M.; Cui, W.; Cai, X.; Zheng, C.; Li, L.; Hu, X.; Zhang, D.; Zhang, J.; Chen, X.; Jiang, W.; Xue, Q. Observation of Unconventional Anomalous Hall Effect in Epitaxial Crte Thin Films. *Nano Research* 2018, 11, 3116-3121.
- 44. Huang, M.; Gao, L.; Zhang, Y.; Lei, X.; Hu, G.; Xiang, J.; Zeng, H.; Fu, X.; Zhang, Z.; Chai, G.; Peng, Y.; Lu, Y.; Du, H.; Chen, G.; Zang, J.; Xiang, B. Possible Topological Hall Effect above Room Temperature in Layered Cr1. 2te2 Ferromagnet. *Nano Lett.* 2021, 21, 4280-4286.
- 45. Wang, Y.; Yan, J.; Li, J.; Wang, S.; Song, M.; Song, J.; Li, Z.; Chen, K.; Qin, Y.; Ling, L. Magnetic Anisotropy and Topological Hall Effect in the Trigonal Chromium Tellurides Cr 5 Te 8. Phys. Rev. B 2019, 100, 024434.
- 46. Zhou, L.; Chen, J. S.; Chen, X. B.; Xi, B.; Qiu, Y.; Zhang, J. W.; Wang, L. J.; Zhang, R. N.; Ye, B. C.; Chen, P. B.; Zhang, X. X.; Guo, G. P.; Yu, D. P.; Mei, J. W.; Ye, F.; Wang, G.; He, H. T. Topological Hall Effect in Traditional Ferromagnet Embedded with Black-Phosphorus-Like Bismuth Nanosheets. ACS Appl. Mater. Interfaces 2020, 12, 25135-25142.
- 47. Zhang, X. Q.; Ambhire, S. C.; Lu, Q. S.; Niu, W.; Cook, J.; Jiang, J. S.; Hong, D. S.; Alahmed, L.; He, L.; Zhang, R.; Xu, Y. B.; Zhang, S. S. L.; Li, P.; Bian, G. Giant Topological Hall Effect in Van Der Waals Heterostructures of Crte2/Bi2te3. Acs Nano 2021, 15, 15710-15719.
- 48. Chen, J.; Wang, L.; Zhang, M.; Zhou, L.; Zhang, R.; Jin, L.; Wang, X.; Qin, H.; Qiu, Y.; Mei, J. Evidence for Magnetic Skyrmions at the Interface of Ferromagnet/Topological-Insulator Heterostructures. Nano Lett. 2019, 19, 6144-6151.
- 49. Saha, R.; Meyerheim, H. L.; Gobel, B.; Hazra, B. K.; Deniz, H.; Mohseni, K.; Antonov, V.; Ernst, A.; Knyazev, D.; Bedoya-Pinto, A.; Mertig, I.; Parkin, S. S. P. Observation of Neel-Type Skyrmions in Acentric Self-Intercalated Cr1+Delta Te2. Nat. Commun. 2022, 13, 3965.
- 50. Zhang, C.; Liu, C.; Zhang, J.; Yuan, Y.; Wen, Y.; Li, Y.; Zheng, D.; Zhang, Q.; Hou, Z.; Yin, G.; Liu, K.; Peng, Y.; Zhang, X.-X. Room-Temperature Magnetic Skyrmions and Large Topological Hall Effect in Chromium Telluride Engineered by Self-Intercalation. *Adv. Mater.* 2023, 35, 2205967.
- Tang, B.; Hu, D.; Zhao, X.; Wang, X.; Liu, Z. Recent Developments in Chemical Vapor Deposition of 2d Magnetic Transition Metal Chalcogenides. ACS Applied Electronic Materials 2022, 4, 3303-3324.
- Sugai, S.; Murase, K.; Katayama, S.; Takaoka, S.; Nishi, S.; Kawamura, H. Carrier Density Dependence of Soft to-Phonon in Snte by Raman Scattering. Solid State Commun. 1977, 24, 407-409
- 53. Wang, J.; Xie, D.; Li, Z.; Zhang, X.; Sun, X.; Coughlin, A. L.; Ruch, T.; Chen, Q.; Losovyj, Y.; Lee, S.; Yu, H.; Zhou, H.; Wang, H.; Wang,

- J.; Zhang, S. Self-Organization of Various "Phase-Separated" Nanostructures in a Single Chemical Vapor Deposition. *Nano Research* **2020**, *13*, 1723-1732.
- 54. Wang, Y.; Qiu, G.; Wang, R.; Huang, S.; Wang, Q.; Liu, Y.; Du, Y.; Goddard, W. A.; Kim, M. J.; Xu, X.; Ye, P. D.; Wu, W. Field-Effect Transistors Made from Solution-Grown Two-Dimensional Tellurene. *Nature Electronics* **2018**, *1*, 228-236.
- 55. Peng, J.; Pan, Y.; Yu, Z.; Wu, J.; Wu, J.; Zhou, Y.; Guo, Y.; Wu, X.; Wu, C.; Xie, Y. Two-Dimensional Tellurium Nanosheets Exhibiting an Anomalous Switchable Photoresponse with Thickness Dependence. *Angew. Chem. Int. Ed.* 2018, 57, 13533-13537.
- Manjón, F. J.; Gallego-Parra, S.; Rodriguez-Hernandez, P.; Munoz, A.; Drasar, C.; Muñoz-Sanjosé, V.; Oeckler, O. Anomalous Raman Modes in Tellurides. *Journal of Materials Chemistry C* 2021, 9, 6277-6289.
- Bahl, M.; Watson, R.; Irgolic, K. X-Ray Photoemission Studies of Tellurium and Some of Its Compounds. *Chem. Phys.* 1977, 66, 5526-5535.
- 58. Neudachina, V.; Shatalova, T.; Shtanov, V.; Yashina, L.; Zyubina, T.; Tamm, M.; Kobeleva, S. Xps Study of Snte (1 0 0) Oxidation by Molecular Oxygen. *Surf Sci.* **2005**, *584*, 77-82.
- Berchenko, N.; Vitchev, R.; Trzyna, M.; Wojnarowska-Nowak, R.; Szczerbakow, A.; Badyla, A.; Cebulski, J.; Story, T. Surface Oxidation of Snte Topological Crystalline Insulator. *Appl. Surf. Sci.* 2018, 452, 134-140.
- 60. Shimada, K.; Saitoh, T.; Namatame, H.; Fujimori, A.; Ishida, S.; Asano, S.; Matoba, M.; Anzai, S. Photoemission Study of Itinerant Ferromagnet Cr1–Δte. *Phys. Rev. B* **1996**, *53*, 7673-7683
- 61. Roy, A.; Guchhait, S.; Dey, R.; Pramanik, T.; Hsieh, C.-C.; Rai, A.; Banerjee, S. K. Perpendicular Magnetic Anisotropy and Spin Glass-Like Behavior in Molecular Beam Epitaxy Grown Chromium Telluride Thin Films. ACS nano 2015, 9, 3772-3779.
- 62. Biesinger, M. C.; Payne, B. P.; Grosvenor, A. P.; Lau, L. W.; Gerson, A. R.; Smart, R. S. C. Resolving Surface Chemical States in Xps Analysis of First Row Transition Metals, Oxides and Hydroxides: Cr, Mn, Fe, Co and Ni. Appl. Surf. Sci. 2011, 257, 2717-2730.
- 63. Citrin, P. H.; Wertheim, G.; Baer, Y. Core-Level Binding Energy and Density of States from the Surface Atoms of Gold. *Phys. Rev. Lett.* **1978**, *41*, 1425.
- 64. Spanjaard, D.; Guillot, C.; Desjonqueres, M.-C.; Tréglia, G.; Lecante, J. Surface Core Level Spectroscopy of Transition Metals: A New Tool for the Determination of Their Surface Structure. Surf. Sci. Rep. 1985, 5, 1-85.
- 65. Biesinger, M.; Brown, C.; Mycroft, J.; Davidson, R.; McIntyre, N. X-Ray Photoelectron Spectroscopy Studies of Chromium Compounds. Surface and interface analysis: an international journal devoted to the development and application of techniques for the analysis of surfaces, interfaces and thin films 2004, 36, 1550-1563.
- 66. Li, Q.; Zhou, Q.; Shi, L.; Chen, Q.; Wang, J. Recent Advances in Oxidation and Degradation Mechanisms of Ultrathin 2d Materials under Ambient Conditions and Their Passivation Strategies. *Journal of Materials Chemistry A* 2019, 7, 4291-4312
- 67. Lee, G.-H.; Cui, X.; Kim, Y. D.; Arefe, G.; Zhang, X.; Lee, C.-H.; Ye, F.; Watanabe, K.; Taniguchi, T.; Kim, P.; Hone, J. Highly Stable, Dual-Gated Mos2 Transistors Encapsulated by Hexagonal Boron Nitride with Gate-Controllable Contact, Resistance, and Threshold Voltage. *ACS nano* **2015**, *9*, 7019-7026.
- 68. Cao, Y.; Mishchenko, A.; Yu, G. L.; Khestanova, E.; Rooney, A. P.; Prestat, E.; Kretinin, A. V.; Blake, P.; Shalom, M. B.; Woods, C.; Chapman, J.; Balakrishnan, G.; Grigorieva, I. V.; Novoselov, K. S.; Piot, B. A.; Potemski, M.; Watanabe, K.; Taniguchi, T.; Haigh, S. J.; Geim, A. K.; Gorbachev, R. V. Quality Heterostructures from

- Two-Dimensional Crystals Unstable in Air by Their Assembly in Inert Atmosphere. *Nano Lett.* **2015**, *15*, 4914-4921.
- 69. Wang, L.; Meric, I.; Huang, P. Y.; Gao, Q.; Gao, Y.; Tran, H.; Taniguchi, T.; Watanabe, K.; Campos, L. M.; Muller, D. A.; Guo, J.; Kim, P.; Hone, J.; Shepard, K. L.; Dean, C. R. One-Dimensional Electrical Contact to a Two-Dimensional Material. *Science* **2013**, *342*, 614-617.
- 70. Bohling, C.; Sigmund, W. Self-Limitation of Native Oxides Explained. *Silicon* **2016**, *8*, 339-343.
- 71. Dowben, P. A.; Wu, N.; Binek, C. When Measured Spin Polarization Is Not Spin Polarization. *J. Phys.: Condens. Matter* **2011**, *23*, 171001.
- 72. Wu, N.; He, X.; Wysocki, A. L.; Lanke, U.; Komesu, T.; Belashchenko, K. D.; Binek, C.; Dowben, P. A. Imaging and Control of Surface Magnetization Domains in a Magnetoelectric Antiferromagnet. *Phys. Rev. Lett.* 2011, 106, 087202.
- 73. Chen, X.; Kazi, H.; Cao, Y.; Dong, B.; Pasquale, F. L.; Santana, J. A. C.; Cao, S.; Street, M.; Welch, R.; Binek, C. Ultrathin Chromia Films Grown with Preferential Texture on Metallic, Semimetallic and Insulating Substrates. *Mater. Chem. Phys.* **2015**, *149*, 113-123.